Using Nonlinear Zeeman Spectroscopy to obtain In-Situ Magnetic Field Measurement in a Hall Thruster

IEPC-2009-088

Presented at the 31st International Electric Propulsion Conference,
University of Michigan • Ann Arbor, Michigan • USA
September 20 – 24, 2009

Wensheng Huang[*], Bailo B. Ngom[†], and Alec D. Gallimore[‡]
Plasmadynamics and Electric Propulsion Laboratory, University of Michigan, Ann Arbor, MI 48109, USA

We present the experimental results based on a novel non-intrusive method for obtaining the magnetic field magnitude profile in a 6-kW Hall thruster operating at the nominal condition. We used the Xe I $6s'[1/2]^0_1 \rightarrow 6p'[3/2]_2$ transition at 834.912 nm (vacuum) to perform laser-induced fluorescence spectroscopy inside the channel near the exit plane. Due to the Zeeman effect, the obtained spectra contain magnetically-split hyperfine structures. A nonlinear error-minimizing solver, utilizing nonlinear Zeeman theory, extracts the magnitude of the magnetic field. A comparison is made between the magnetic field strength in air, which is measured via a Hall probe, and the in-situ magnetic field strength to study the effects of the self-field induced by the Hall current. The magnetic field is found to be weaker than its air value around the middle of the thruster channel in the interrogated axial positions but matches air values very well near the wall. The differences are found to vary by as much as 30 Gauss. The uncertainty analysis that follows helps identify the strengths and weaknesses of this technique for in-situ magnetic field measurements in Hall thrusters.

I. Introduction

ALTHOUGH many Hall thrusters have flown on satellites and flight models are now commercially produced in the United States there are still many unanswered questions about the fundamental physics of Hall thruster operation. One of these outstanding questions is related to the effect of the self-magnetic-field produced by the Hall current. The Hall current has been measured and approximated in the past using probes; measurements show the total Hall current is typically 4 to 5 times as large as the discharge current.[1] However, due to perturbative effects associated with probes in the channel of a Hall thruster and the limited number of studies, the Hall current's exact strength and distribution is unclear. A sufficiently concentrated Hall current can produce a significant self-magnetic-field that will alter the shape and strength of the local magnetic field. It has been shown that Hall thrusters with a magnetic lens topology that is symmetric about the channel centerline tend to confine the plasma better and have better performance than thrusters with an asymmetric field.[2] However, without in-situ magnetic field measurements, it is difficult to be certain that the field is symmetric when the thruster anode efficiency is maximized. Furthermore, it is difficult to assess how much of an effect the self-magnetic-field may have in distorting the field symmetry. Peterson et al. used a B-dot probe that can rapidly extend into and retract from a Hall thruster's channel.[3] However, the uncertainties in the results were difficult to characterize due to the perturbation to the plasma induced by the probe.

This paper describes a novel experimental approach to obtain the magnetic field magnitude in a Hall thruster non-intrusively by taking advantage of the Zeeman effect. With the right setup, this method can also be used to obtain magnetic field components. The nonlinear Zeeman theory used in this experiment is based on a combination of experimental and theoretical studies previously presented.[4-6] When a laser beam interacts with a particle in an

[*] Ph. D. Candidate, Aerospace Engineering, davhuang@umich.edu.
[†] Ph. D., Aerospace Engineering, bbahn@umich.edu.
[‡] Arthur F. Thurnau Professor, lab director, Aerospace Engineering, Alec.Gallimore@umich.edu.

externally applied magnetic field, the particle's excitation levels split into multiple energy levels. The exact frequency shift and amplitude of these magnetically split spectral lines are dependent on both the magnitude of the magnetic field and the direction of the field line with respect to the laser beam polarization vector. When the splitting is induced by a weak magnetic field (< few hundred Gauss), it is called the Zeeman effect. When the magnetic field is strong (> few thousand Gauss), the phenomenon is called the Paschen-Back effect. The magnetic fields of many Hall thrusters have regions with strengths that fall in the transition region and require the full magnetic hyperfine theory to describe. The solver used to solve for the magnetic field iteratively estimates the field strength and refines the solution based on the difference between the theoretically calculated spectrum and the raw spectrum. [6] Greater details can be found in the theory section.

II. Theories

Subsection A describes the principles of laser-induced fluorescence (LIF) measurement. Subsections B and C describe the theories of how the magnetic field influences the spectra obtained from LIF. Subsection D provides a basic description of the Hall current in a Hall thruster and a rough estimate of how much influence it can have. Subsection E provides a basic description of the diamagnetic current in a Hall thruster. Since the present study focus on atomic xenon, the theories in this paper will deal only with atomic spectroscopy.

A. Principles of Laser-Induced Fluorescence and the Doppler Effect

LIF operates on the principle that an atom will absorb a photon of a certain frequency, become excited, and de-excite by spontaneously emitting another photon. This spontaneous emission, called fluorescence, radiates isotropically away from the particle. The exact frequency for which photons will be absorbed depends on the quantum mechanical characteristics of the electrons and nucleons in the particle. By varying the frequency of the injected photons and comparing the intensity of the collected fluorescence we can obtain raw LIF traces of the transition of interest at the interrogation zone. In this experiment, light is injected at around 834.9 nm and non-resonant fluorescence is collected at 473.415 nm (air). Figure 1 shows the corresponding transition diagram.

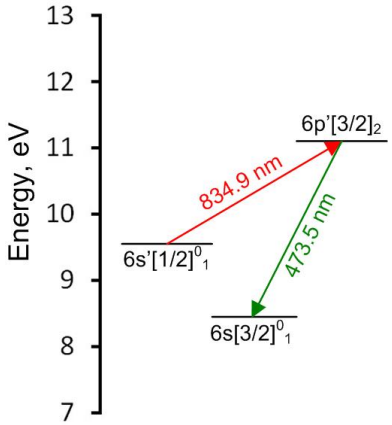

Figure 1. Transition diagram for this study. *Wavelengths in vacuum*.

Though the quantum nature of photon-atom interaction suggests that all transitions should have fixed energies, and therefore fixed wavelengths, real LIF spectra are broadened by a number of natural phenomena. The most common broadening effect is due to kinetic motion; this is called the Doppler effect. Atoms absorb photons at a shifted frequency if the atoms are moving with respect to the photon travel axis. The shift in absorption frequency is proportional to the velocity of the atom in the direction of the laser beam axis. For LIF velocimetry, this effect is used to obtain velocity distribution functions (VDF), an example study of which can be found in Ref. 7. However, for the present study, the Doppler effect can interfere with the solvers ability to calculate the magnetic field strength.

The Xe I 834.9 nm transition was chosen for this study because in a Hall thruster environment xenon neutrals typically have Maxwellian-like VDFs with low temperatures (600-1000 K) and low bulk velocities (100-300 m/s).[8] Thus, an approximate description of the Doppler broadening depends only on one parameter, the temperature, as long as one shifts the frequency axis to cancel out the effect of the bulk velocity. Having a low temperature is advantageous because high temperature (>5000 K) Doppler broadening, as found in Hall thruster xenon ion population, smoothes out magnetically-split hyperfine structures. The solver simultaneously solves for the magnetic field strength and the temperature to account for the effects of Doppler broadening. The Xe I 834.9 nm transition is also useful in that it is readily accessible by current diode laser technology. However, the lower state of the transition is not metastable so the signal-to-noise ratio (SNR) tends to be low outside the thruster.

B. Hyperfine Structure and Natural Broadening

Another prominent broadening factor for xenon is hyperfine structure. These structures normally add large distortions to the raw data, but they can be taken advantage of to extract information about the magnetic field. The hyperfine structures show up as multiple distinct spikes in the spectrum of a cold (T = 0 K) gas where there would normally only be one spike.

The hyperfine structure is a result of two types of atomic-level effects. The first type is associated with the interactions between the intrinsic spin of the nucleus and the electric and magnetic fields associated with the total

electron angular momentum. The most prominent intrinsic electric interaction is called the electric quadrupole interaction, which is small for the Xe I 834.9 nm transition. The most prominent intrinsic magnetic interaction is called the magnetic dipole interaction. The physics of how this interaction changes under the application of an external magnetic field is the basis for Zeeman spectroscopy. More details about the magnetic hyperfine effect can be found in the next sub-section. The second type of effect, called the isotopic shift, is due to minute differences in the masses and electron orbital shapes of different isotopes. This topic is dealt with in greater detail by Svanberg.[9]

To simplify calculations when dealing with hyperfine structures, there are constants associated with each of the effects listed above. Together, they are called the hyperfine structure constants. The hyperfine structure constants for the Xe I $6s'[1/2]^0_1 \rightarrow 6p'[3/2]_2$ transition are well established.[10, 11]

Additionally, externally applied electric fields can induce hyperfine structure splittings. This effect is called the Stark effect. The electric field present in a typical Hall thruster is several orders of magnitude smaller than what is necessary to cause a detectable frequency shift in xenon.[12]

Natural (or lifetime) broadening is also present to complicate the analysis of LIF spectra. Natural broadening can be explained by the Heisenberg uncertainty principle. Since energy and temporal measurements are complementary, we cannot know with absolute certainty the exact energy of a photon emitted from a particle whose decay time is uncertain. The result is that even if all other circumstances are equal, no two photons from the same de-excitation will be measured with exactly the same energy. This effect broadens an absorption line into a Lorentzian function. The lifetime constant for the Xe I $6s'[1/2]^0_1 \rightarrow 6p'[3/2]_2$ is also well established.[13]

C. Magnetic Hyperfine Effect

The effect of applied magnetic fields on hyperfine structure is typically categorized as the Zeeman effect for low field strength (< few hundred Gauss) and the Paschen-Back effect for high field strength (> few thousand Gauss). The magnetic fields of many Hall thrusters have strengths that fall in the transition region and require the full magnetic hyperfine theory to describe. This type of interaction is sometimes called the nonlinear Zeeman effect.

The interaction of photons with particles under the influence of external magnetic field is also categorized under σ- and π-polarization. The laser beam is σ-polarized if the polarization of the beam is perpendicular to the external magnetic field (**E** ⊥ **B**). The beam is π-polarized if the polarization of the beam is parallel to the external magnetic field (**E** || **B**). For the Xe I 834.9 nm transition, π-polarized splittings are at least an order of magnitude narrower than σ-polarized splittings.[5] This difference gives rise to an effective tool for determining field direction.

Since the σ-component splitting is perpendicular to the magnetic field line, the associated field strength result is in a plane perpendicular to the field line at the interrogation location. For this reason we can normally only resolve two components of the magnetic field. However, the cylindrically-symmetric magnetic field of a typical Hall thruster can ideally (barring machining asymmetry) be described by two magnetic field components. Thus, for a typical Hall thruster, the magnetic field direction can be mapped using a transition line with a strong difference in its hyperfine structure splitting when interacting with σ- versus π-polarized light. Figure 2 shows simulated Xe I 834.9 nm spectra with 0 G versus 200 G of externally applied magnetic field when the atoms are interrogated with a σ-polarized laser. The π-polarized interaction is so weak that the B = 0 G, σ-polarized spectrum looks essentially the same as a B = 200 G, π-polarized spectrum for typical neutral temperatures found in Hall thrusters.

This study is primarily focused on demonstrating the use of nonlinear Zeeman spectroscopy in Hall thruster and will focus on measuring magnetic field strength instead of direction. By maximizing the amount of σ-interaction,

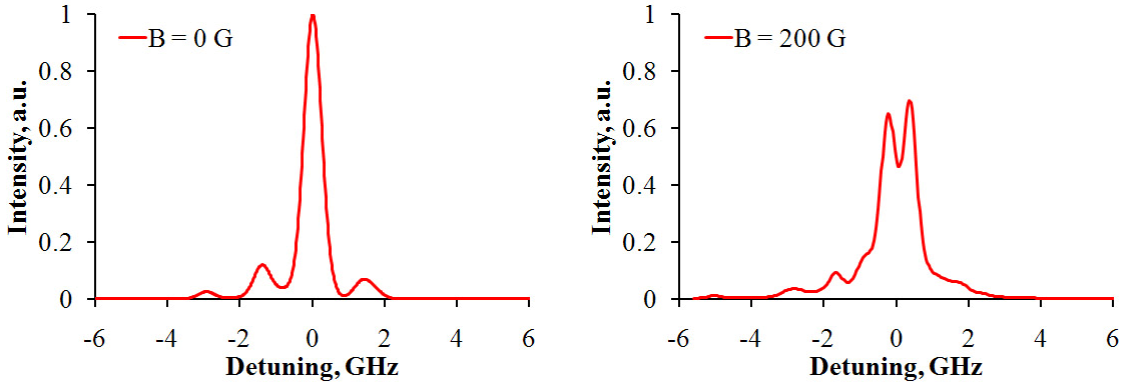

Figure 2. Simulated warm (~600 K) Xe I 834.9 nm σ-polarized hyperfine structure lineshapes under external applied magnetic field of strengths 0 G (left) and 200 G (right). *Wavelength in vacuum.*

and minimizing π- interaction, the resulting LIF traces show more prominent splitting and are easier for the solver to analyze. We can accomplish this by pointing the polarization vector in the azimuthual direction so that all interactions are σ-interactions. In this configuration, the measured hyperfine splitting is associated with the magnitude of the magnetic field in the axial-radial plane.

This study is a continuation of a previously published work by Ngom, et al.[6] The full theory for determining the amount of splitting and the amplitude of the resulting hyperfine transition lines are described in the said work.

Also described in Ref. 6 is the solver used for this study. This solver is based on a commercial solver in MATLAB® designed for solving nonlinear problems. Details about the specific algorithm used can be found in Ref. 14. The magnetic field solver pose the problem of finding the magnetic field strength as an error minimization problem, where the error is the sum of the square of the difference between the LIF data points and the simulated spectra. When the error is minimized, the simulated spectra, whose magnetic field strength is known, will be as closely matched to the LIF spectra as possible.

At this point, the magnetic hyperfine theory brings up another possibility for how to carry out Zeeman spectroscopy in a Hall thruster. Instead of collecting only σ-polarized spectra we can collect both σ- and π-polarized spectra, use the π-polarized spectra to calculate the VDF (or the temperature if the VDF is Maxwellian), then use the magnetic field solver on the σ-polarized spectra to solve for only the magnetic field. The advantage of this approach is that the VDF (or the temperature) will already be known, eliminating one of the variables the solver needs to solve for, and improving the fidelity of the magnetic field result. The disadvantages of this approach are the need to take twice as many scans per interrogation location, and the difficulty of obtaining π-polarized traces without a priori knowledge of the field direction. We chose not to use this approach since we do not know how the Hall current changes the local field direction.

D. Hall Current in the Hall Thruster

The Hall thruster has a very high ionizing efficiency primarily because it is able to trap electrons (but not ions) into an azimuthual current called the Hall current. The Hall current arises as a result of the mostly axial electric field and the mostly radial magnetic field in the ionization and acceleration zones of the Hall thruster. The associated ExB drift in the azimuthual direction gives rise to a current loop composed of only electrons in an annular Hall thruster. This current loop generates a self-magnetic-field that either adds or subtract from the local magnetic field depending on location.

The Hall current has not been directly measured. Doing so with a probe will interrupt the Hall thruster's operation and invalidate any collected data. Indirect measurement of the Hall current typically uses electric fields measured from an emissive probe, magnetic fields measured from a Hall probe in air, and electron or ion densities measured from some form of Langmuir probe. The results are combined via Eq. (1) to obtain the Hall current,

$$\mathbf{j}_{ExB} = en_e \mathbf{u}_{ExB} = en_e \frac{\mathbf{E} \times \mathbf{B}}{B^2} \tag{1}$$

where $\mathbf{j}_{ExB}$ is the ExB current density, e is the elementary charge, n_e is the electron density, $\mathbf{u}_{ExB}$ is the ExB drift velocity, **E** is the electric field, and **B** is the magnetic field. Since probes are involved, it is difficult to characterize the uncertainty associated with measuring the Hall current this way.

Nevertheless, we can use probe data as a starting point for predicting what kind of influence the Hall current will have on the magnetic field. Assuming the Hall current is roughly concentrated in a loop of cross-sectional radius r_0 and the total current going through is I_0, the highest magnetic field strength induced by the Hall current outside the loop can be calculated by Eq. (2),

$$B_{max} = \frac{\mu I_0}{2\pi r_0} \tag{2}$$

where μ is the fluid permeability. From probe measurements by Haas and Gallimore,[1] the Hall current is 4-5 times the discharge current in a thruster similar to the one tested for this study. Given a nominal operating current of 20 A, we will approximate the total Hall current as on the order of 100 A. Using the vacuum permeability, we can now calculate roughly what kind of distortion to the local magnetic field we should expect for a given Hall current cross-sectional radius. For a Hall current roughly the size of the acceleration zone (~20 mm[7]), B_{max} is ~10 Gauss. Furthermore, B_{max} is inversely proportional to the Hall current cross sectional radius and proportional to the total

Hall current. The more concentrated the Hall current is, the higher B_{max} will be. The above analysis is at best an order of magnitude analysis, but it does give us an idea of what to expect when measuring the distortion to the magnetic field induced by the Hall current.

E. Diamagnetic Current in the Hall Thruster

As the name implies, the diamagnetic current produces a self-field that strictly decreases the local magnetic field strength. This current comes about because free floating charged particles in an externally applied magnetic field naturally gyrate in such a way that the net resulting current produces a self-magnetic field that opposes the applied field. Like the Hall current the diamagnetic current is mostly azimuthual in a Hall thruster, but unlike the Hall current the diamagnetic current travels in both directions and the net current summed across the entire physical domain is always zero. Equation (3) shows how the diamagnetic current in a Hall thruster can be calculated,

$$\nabla\left(n_e k T_e\right) = \mathbf{j}_{dia} \times \mathbf{B} \tag{3}$$

where k is the Boltzmann constant, T_e is the electron temperature, and $\mathbf{j}_{dia}$ is the diamagnetic current density . Previous calculations using internal probe data shows that the strength of the diamagnetic current is roughly an order of magnitude less than that of the Hall current.[15] We will compare the strengths of the Hall and diamagnetic currents in the results section to get a better idea of how important one is versus the other.

III. Experimental Setup

Subsections A-E describe the LIF experimental setup.

A. Facility

Experiments were performed in the Large Vacuum Test Facility (LVTF) of the Plasmadynamics and Electric Propulsion Laboratory (PEPL) at the University of Michigan. The LVTF is a φ6 m × 9 m stainless steel-clad cylindrical chamber. Due to the size of the chamber, the thruster plume is able to expand un-impeded until termination at a beam dump ~4 m downstream. Pumping is provided by seven cryopumps with a nominal xenon pumping speed of 245,000 l/s. Facility pressure is monitored by two hot-cathode ionization gauges. The base pressure is approximately 2×10^{-7} Torr. The pressure during thruster operation at 20 mg/s anode mass flow rate is approximately 9×10^{-6} Torr, corrected for xenon.

During the experiments, the 6-kW Hall thruster was mounted on two cross-mounted stepper-motor translation stages. The stages provide 1 m of axial travel and 2 m of radial travel accurate to within 0.01 mm. Laser injection and LIF collection optics were fixed to the floor of the chamber.

Research-grade xenon propellant (99.999% pure) was supplied to the thruster by commercially available flow meters and controllers, having an accuracy of ±1%. Calibration of the flow system was done by the constant volume method taking into account the effects of compressibility.

B. Thruster

The 6-kW annular Hall thruster nominally operates at a discharge voltage of 300 V and an anode mass flow rate of 20 mg/s. Cathode mass flow rate is fixed to 7% of the anode mass flow rate. Magnetic field settings are chosen to create roughly a symmetric magnetic field (about the thruster channel centerline) and to maximize thruster efficiency. These settings were found through the use of an inverted pendulum thrust stand. The nominal operating condition was used for the entirety of this study.

C. Laser and Air-Side Injection Optics

Figure 3 shows the air-side laser and optics setup for the LIF experiment. The laser system used is a TOPTICA TA-100/830 tapered-amplifier diode laser. This system has a nominal linewidth of ~10 MHz and a mode-hop-free range of ~12 GHz. Output power is ~250 mW at the wavelength used in this study.

Two relatively weak beams are split off from the main laser beam and sent into the Burleigh SA-91 etalon assembly (2 GHz free spectral range, finesse >300) and the Burleigh WA-1000 wavemeter (accurate to 1 pm) for reference information. A third relatively weak beam is split off and sent into the optogalvanic cell for stationary reference. This beam is mechanically chopped at ~1.1 kHz.

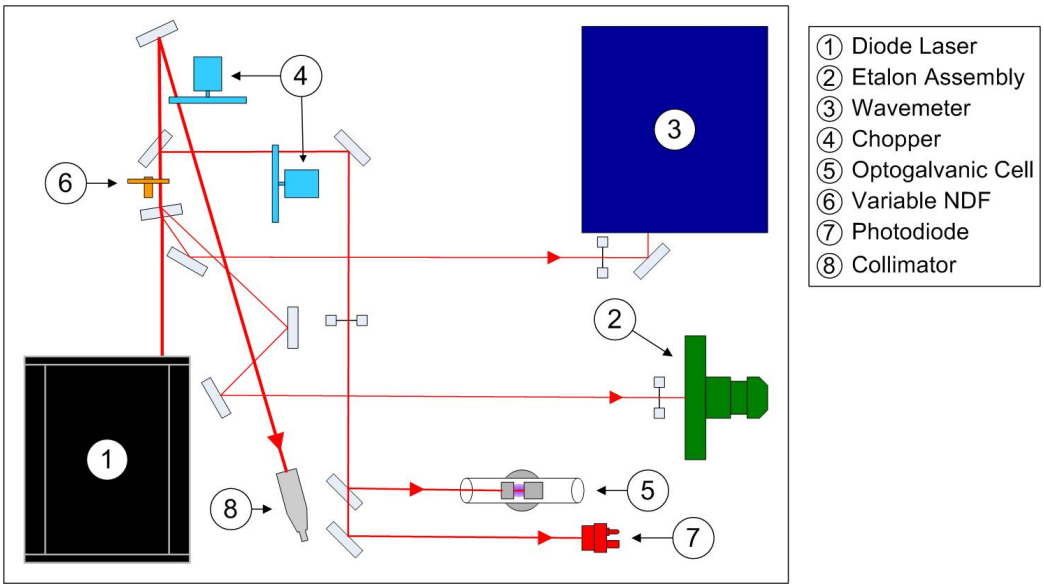

Figure 3. Air-side laser injection setup.

The optogalvanic cell used in this study is a Hamamatsu L2783-42 XeNe-Mo galvatron. The core of the galvatron is a pair of φ6.25 mm cylindrical Mo tube electrodes centered in a φ25 mm x 120 mm glass cylinder. The cylinder is filled with approximately 3 Torr of xenon and 4 Torr of neon. The ends of the cylinder are angled at approximately 10 degrees from being perpendicular to the electrode axis to eliminate retro-reflection. The galvatron is operated at 250 V to maintain a warm, dense, and stationary plasma rich with ion species. The voltage drop across the cell's ballast resistor is connected to a SR-810 lock-in amplifier through an RC filter that passes only the AC component of the signal.

A fourth weak beam is split into a Thorlabs DET-110 photodiode to monitor laser power drift. This reading is fed into another SR-810 lock-in amplifier for signal collection. For a relatively unsaturated LIF trace, this laser power reading is used to remove the effects of laser power drift from the trace.

The remaining beam power is mechanically chopped at ~1.8 kHz via an SR540 chopper, and sent into a fiber collimator. The fiber delivers the light through an optical feedthru into the vacuum chamber.

When doing a saturation study, an additional variable neutral density filter is added so that the laser power being injected into the chamber can be fine tuned.

D. Vacuum-Side Optics

Figure 4 shows a diagram of the vacuum-side experimental setup. The injection optics send the laser beam axially into the thruster. This beam is focused down to a point with a 1-mm diameter circular cross section via an anti-reflection-coated plano-convex lens. A polarizer (not shown in diagram) is placed between the optical fiber output and the lens to provide horizontal polarization with respect to the chamber floor. The injection beam focusing cone has a half-angle of ~0.5° and the injection axis is aligned to within 0.1° of the thruster firing axis so cosine losses are negligible. The interrogation zone is at the 9 o'clock position when viewing the thruster face-on so the local magnetic field is in a plane roughly parallel with the chamber floor. To obtain pure σ-polarized LIF spectra, the laser beam polarization vector needs to be vertical. To prevent excess beam drift during thruster operation an optics shield is installed to allow the laser through while blocking the incoming xenon particles.

The collection optics is built from a matching pair of anti-reflection-coated achromatic lenses. Prior thermocouple measurements showed that thermal shielding is not necessary for the collection optics. Nevertheless, some thermal drift takes place over the course of the test so a reference pin is installed to the left of the thruster viewed face-on. The exact position of this pin relative to the thruster is known and the reflected laser signal from this pin is used to compensate for thermal drift.

Four experimental trials were performed instead of one for two reasons. First, we were learning how to better obtain data from inside the thruster channel with each successive trial. Second, it is impossible to obtain data from right next to both the inner and outer walls inside the channel with only one setup. Figure 4 shows the three configurations we used to obtain the data that will be presented later. Figure 4a shows the setup for interrogating across the channel at the exit plane (Experiment #1). This experiment was the initial setup to examine whether we

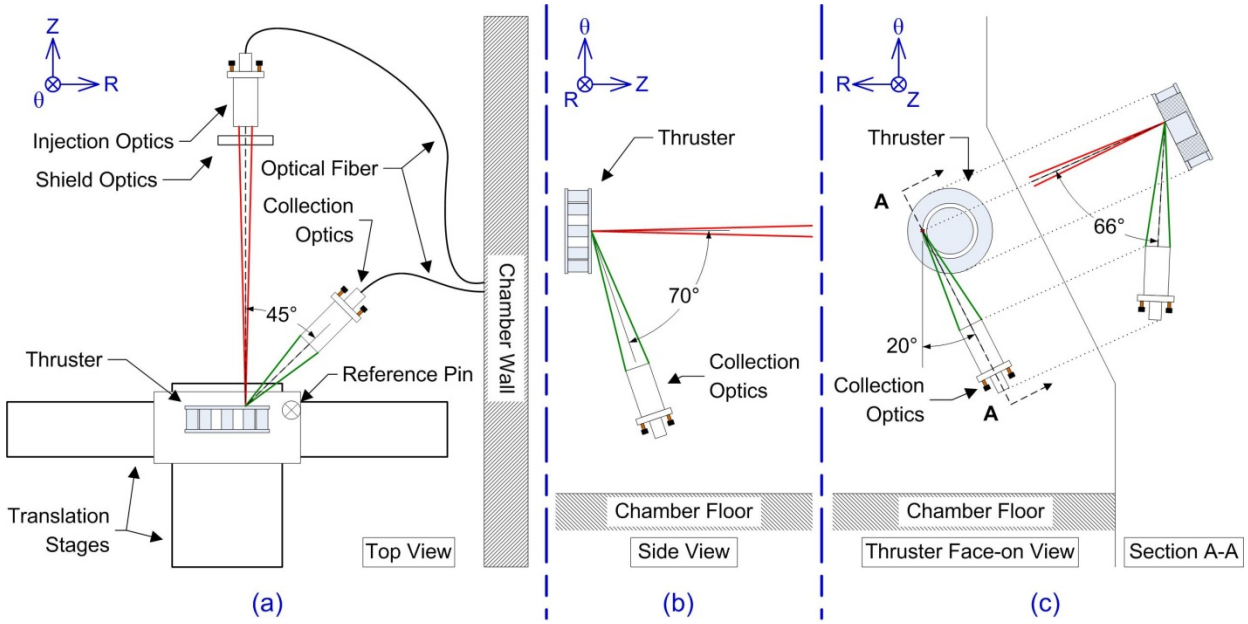

Figure 4. Vacuum-side experimental setup. *Sub-figure (a) depicts the setup for experiment 1. Sub-figure (b) depicts the setup for experiment 2. Sub-figure (c) depicts the setups for experiment 3 and 4.*

can obtain LIF traces with high enough SNR for Zeeman spectroscopy. Figure 4b shows the configuration used to obtain data near the inner wall (Experiment #2). Figure 4c shows the setup used to obtain data near the outer wall (Experiment #3) and the middle (Experiment #4) of the channel.

Since LIF data were collected across multiple experimental trials, great care was taken to ensure the thruster operated under the same condition for all trials. The biggest uncertainty in matching the operation parameters was the anode mass flow rate at ±1%. All collection optics angles were aligned to within 1°. The interrogation zones for all setups were ~1.5 mm in diameter. This dimension sets the spatial resolution of the LIF measurements.

E. Air-Side Collection Optics

An optical fiber brings the fluorescence signal from the chamber to a SPEX-500M monochromator, the output of which is amplified by a Hamamatsu R928 photomultiplier. The amplified signal is sent to a third SR-810 lock-in amplifier. A slit size of 1 mm, corresponding to an optical bandwidth of 1 nm, was used.

IV. Data Analysis and Results

A. Data Analysis

Figure 5 shows the saturation study plot for this study. It is important that the LIF data is relatively unsaturated, as shown, because saturation effect changes the relative intensity between the peaks in an LIF trace. This distortion can negatively impact the magnetic field solver's ability to converge on the right solution.

The first step in the data analysis process is to convert the outputs from the various instruments listed in the experimental setup section into a trace of intensity versus detuning, i.e. relative spectral frequency. Next, the detuning of each raw LIF trace is shifted so that the average frequency of the trace is zero. This action is equivalent to removing the Doppler shift associated with the neutral xenon bulk velocity and thus reduces the number of variables the solver has to solve for by one. Finally, the nonlinear Zeeman solver takes over. Due to the presence of

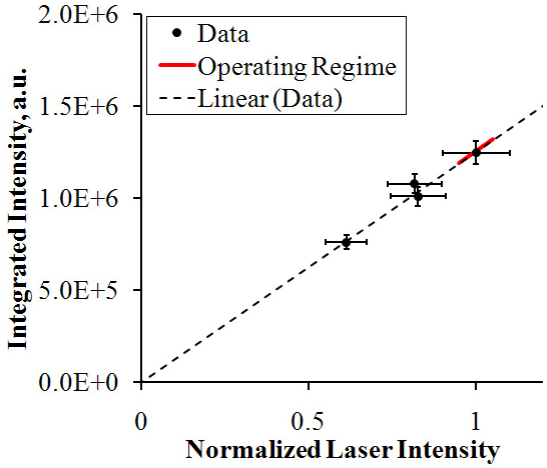

Figure 5. Saturation plot for this study.

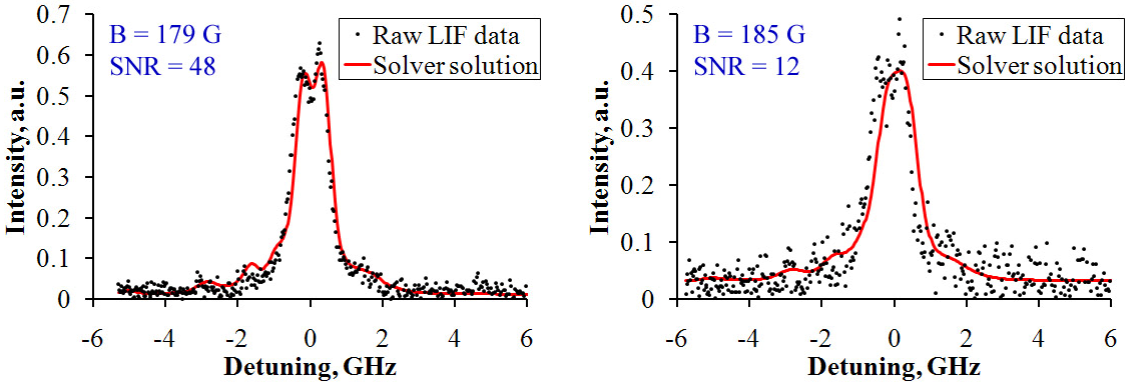

Figure 6. Sample comparisons of raw data versus spectra simulated using solver solutions. *The plot shows that the solver is able to obtain a much better fit for high SNR data (left) than for low SNR data (right).*

noise, which shows up as a floor for non-phase-sensitive lock-in in a SR-810, an additional variable was used in the Zeeman solver. This variable represents the magnitude of the noise and is roughly equal to the root-mean-square of the noise fluctuation. Although adding this extra variable extends the solver convergence time, it does provide a simple means of calculating the signal-to-noise ratio, shown in Eq. (4). To ensure this definition of SNR does not depend on intensity scaling, traces are normalized by the amplitude of the tallest peak before the SNR is calculated.

$$\mathrm{SNR} \equiv \frac{\text{Amplitude of tallest peak}}{\text{Root mean square of noise}} = \frac{1}{\mathrm{Noise}_{\mathrm{RMS}}} \tag{4}$$

Figure 6 compares the performance of the solver when used on raw traces of different SNR. We can see from this figure that the solver performs much better when the data's SNR is high. We assign an arbitrary cutoff of 25 for deciding whether the SNR of a trace is high enough because all traces that meet the cutoff fit more like the high SNR subfigure in Fig. 6 than the low SNR subfigure. Results from traces that do not meet the cutoff are not shown.

In order to isolate the effect of the Hall current, the LIF in-situ magnetic field strength measurements were subtracted from the in-air Hall probe measurements. Given the small difference in permeability between air and vacuum, the in-air measurements are a good estimate of the thruster's vacuum magnetic field. Any difference between the vacuum field and the in-situ measurements is presumably caused by the Hall current.

Due to the finite dimensions of the Hall probe, it turns out in-air field measurements can only reach so close to the wall such that there are no in-air measurements to compare the near-wall in-situ measurements against. For this reason, only data from experiment 1 and 4 are used in the comparison.

It was discovered in a previous work[6] that for the typical neutral temperatures in a Hall thruster and a σ-polarized laser beam, there is a minimum magnetic field strength for which the solver gives a correct value. Below this threshold, the magnetic splitting becomes small enough, compare to the Doppler broadening, that the solver will consistently under-predict the field strength. This threshold turns out to be about 100 G. If the solver returns a value lower than 100 G, we set the value to 100 G with the understanding that it could actually be lower than 100 G. For these data points, extra wide error bars are used.

Note that all axial positions are normalized against discharge channel length and negative axial positions are inside the channel. Normalized axial position is assigned the variable Z. The exit plane is located at Z = 0 and the anode is located at Z = -1. Radial positions are normalized against discharge channel width. Normalized radial positions are assigned the variable R. The inner wall is located at R = 0 while the outer wall is located at R = 1.

B. Uncertainty Analysis

Since this technique is being used in a Hall thruster environment for the first time, it is difficult to assess the uncertainty without more data. However, we can use a simple engineering approach to obtain a rough estimate for the uncertainty in the measured magnetic field. Since the solver relies on error minimization, it will try to obtain a simulated lineshape with a width as close as possible to the width of the raw data (Fig. 6). The solver does this because even a small amount of error in the width of the spectrum will lead to large difference in the intensity value between the simulated spectrum and the raw data, which is further exaggerated when the square of the error is computed to derive the error energy. The end result is that the two rapidly rising/falling parts of the raw data

contributes more to the error energy than any other parts if they are not fitted correctly. Figure 7 shows the two parts in question. The described trend allows us to calculate the approximate influence that the signal-to-noise ratio has on the fidelity of the magnetic field. Equation (5) shows how the root-mean-square of noise contributes to the uncertainty in detuning,

$$\Delta\upsilon_{noise} \approx \frac{\partial\upsilon}{\partial L} * \mathrm{Noise}_{RMS} \tag{5}$$

where $\Delta\upsilon_{noise}$ is the contribution to detuning uncertainty due to noise in the intensity, $\partial\upsilon/\partial L$ is the change in detuning per unit change in intensity due to noise, and Noise_{RMS} is the uncertainty in intensity due to noise. The parameter $\partial\upsilon/\partial L$ is approximated as the average of the magnitudes of the slopes found in the signal at half the height of the maximum signal, shown in the blue circles in Fig. 7.

There are three major sources of error that can contribute to the uncertainty in the detuning. The first of these is the uncertainty in detuning due to equipment resolution and post-processing. The second is the uncertainty due to noise in the intensity as described above. The third is the uncertainty due to the solver converging on the incorrect temperature.

It turns out for magnetic field strengths above 100 G and neutral temperatures expected in a Hall thruster, the magnetic field strength solution is relatively insensitive to the temperature. This can be seen in the large fluctuation in temperature (±50 K out of 500 K) obtained during the calibration study[6] even though the actual neutral temperature did not change from trace to trace. Nevertheless, the solver converges on the correct magnetic field reliably even when the temperature solution fluctuates. Additionally, it is difficult to judge how much of an effect an erroneous temperature will have on the magnetic field solution, so this component of error is ignored for the time being. Assuming the two remaining sources of error are statistically independent, Eq. (6) shows the total uncertainty can be calculated as,

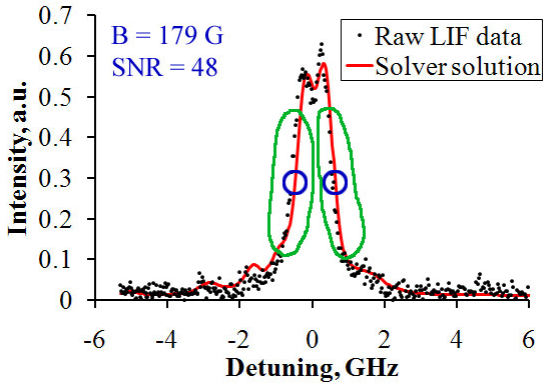

Figure 7. Parts of the LIF trace that have the most influence on the solver. *Influential parts circled in green.*

$$\Delta\upsilon_{total} \approx \sqrt{\Delta\upsilon_{noise}^{\,2} + \Delta\upsilon^{2}} \tag{6}$$

where $\Delta\upsilon_{total}$ is the total uncertainty in detuning, $\Delta\upsilon_{noise}$ is calculated from Eq. (5), and $\Delta\upsilon$ is the equipment contribution, which is primarily limited by the scanning frequency resolution to 30 MHz. The parameter $\Delta\upsilon_{noise}$ is computed on a scan-by-scan basis. The result is converted to uncertainty in magnetic field strength by using Eq. (7),

$$\Delta B \approx \frac{\partial B}{\partial\upsilon_{FWHM}} * \Delta\upsilon_{total} \tag{7}$$

where ΔB is the uncertainty in the magnetic field strength and $\partial B/\partial\upsilon_{FWHM}$ is the change in magnetic field strength per unit change in full-width-at-half-maximum (FWHM) detuning. This equation is accurate because the solver determines magnetic field strength by first matching the width of the lineshape and because the solver is insensitive to temperature changes for the LIF transition we used. We can obtain $\partial B/\partial\upsilon$ by plotting the magnetic field strength versus the FWHM detuning for the collected data, perform a linear fit, and extract the slope of the fit. This process is shown in Fig. 8.

Once we obtain the uncertainty in the magnetic field strength, we then multiply it by an engineering margin of 1.5 to account for any other sources of uncertainty that were not included. Interestingly, the final results show that with the traces deemed usable in this study (SNR > 25, B > 100 G), the uncertainty in magnetic field strength varies from 9-13 G. To be more precise, traces with SNR between 25 and 50 exhibit a projected uncertainty of 10-13 G, while traces with SNR of 50-300+ have 9-10 G of uncertainty. This trend suggests that a SNR of 25 was indeed a

good cutoff for usable LIF traces. Furthermore, for traces with SNR >50, the equipment resolution becomes the dominant source of uncertainty.

As mentioned earlier, traces that yield less than 100 G when processed by the solver are set to 100 G with the understanding that the in-situ field strength can be lower. The error for these data points are assigned as double the calculated uncertainty.

Note that the uncertainty associated with having a finite interrogation zone size was not taken into account rigorously. That is because doing so requires more knowledge about the local magnetic field gradient. However, we project this error to be relatively small in comparison to what is calculated above because field gradients are relatively small in the interrogated regions.

The uncertainty in the magnetic field strength measured in air by the Hall probe is ±0.025%, which translates to less than 1 G for all recorded field strengths.

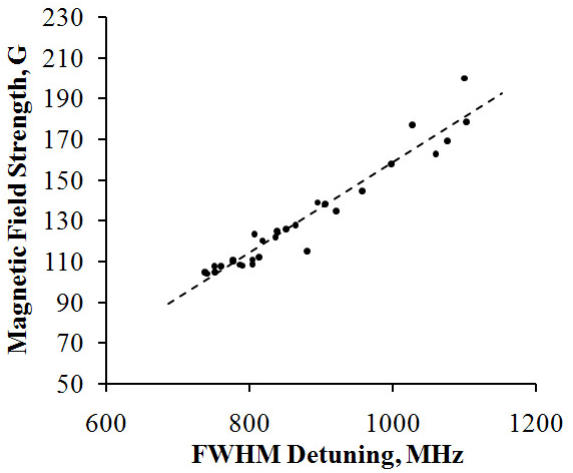

Figure 8. Magnetic field strength calculated by the solver versus FWHM detuning.

C. Results

Figure 9 shows the normalized in-situ magnetic field strength as a function of normalized spatial coordinates. The magnetic field strengths are normalized against the highest measured magnetic field strength. The field strength values in the region for which no usable data were obtained are set to 0 and displayed in blue. Dashed boundary lines mark the regions in which usable data were obtained.

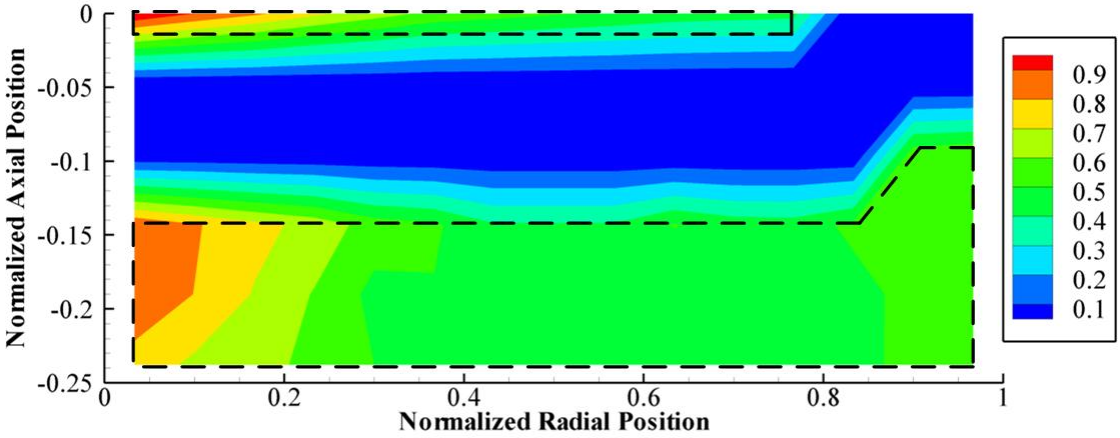

Figure 9. Normalized in-situ magnetic field strength. *Magnetic field strengths normalized by peak magnetic field strength. Axial position is normalized by the channel length with the channel exit plane at 0 and the anode at -1. Radial position is normalized by the channel width with the inner wall at 0 and the outer wall at 1. Marked out in dashed boundaries are the regions where usable data were collected.*

For the remainder of this paper, we define the field strength deficit as the in-air minus the in-situ magnetic field measurement. We do this because the in-situ field strengths turn out to be almost exclusively lower than the in-air field strengths. This definition gives almost all positive values for the field strength difference and is easier to plot. Figures 10-13 show the field strength deficit as a function of radial location at different axial locations. Due to a technical problem with the diode laser, no useable data were collected for Z = -0.048 and Z = -0.095. Any data point where the in-situ field strength is cut off at 100 G due to the solver's detection threshold is circled in red. The associated error bar is also larger than usual. Given the definition of field strength deficit, cutting the in-situ field strength off at 100 G means the deficit is most likely larger than what is calculated for these specially-treated data points.

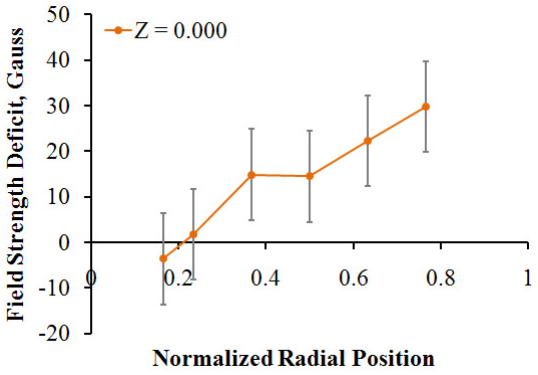

Figure 10. Field strength deficit profile at Z = 0.

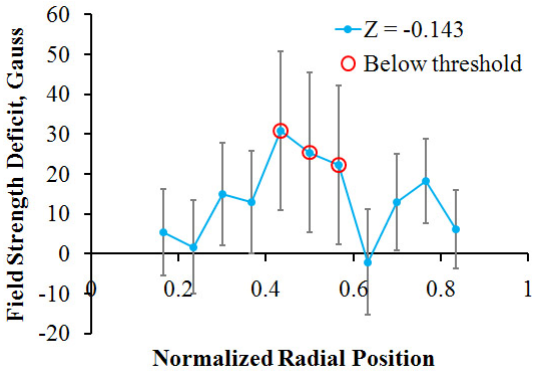

Figure 11. Field strength deficit profile at Z = -0.143.

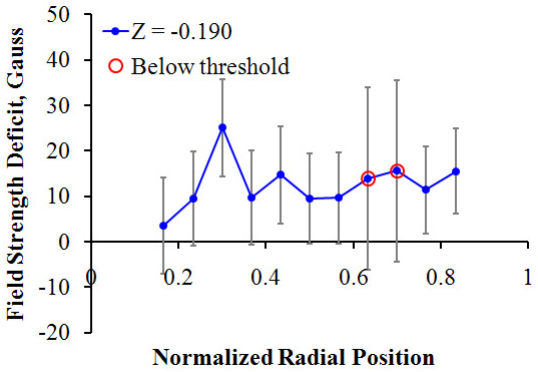

Figure 12. Field strength deficit profile at Z = -0.190.

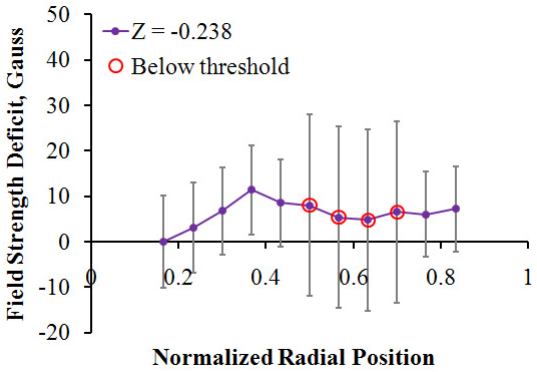

Figure 13. Field strength deficit profile at Z = -0.238.

Field strength deficit is defined as the in-air minus the in-situ magnetic field strength. Red circles denote traces that yielded <100 G for the in-situ magnetic field and have been cut off at 100 G. Based on the definition of the field strength deficit, this means the real difference in magnetic field strength is most likely greater than what is displayed for these data points. Axial position is normalized by the channel length with the exit plane at 0 and the anode at -1. Radial position is normalized by the channel width with the inner wall at 0 and the outer wall at 1.

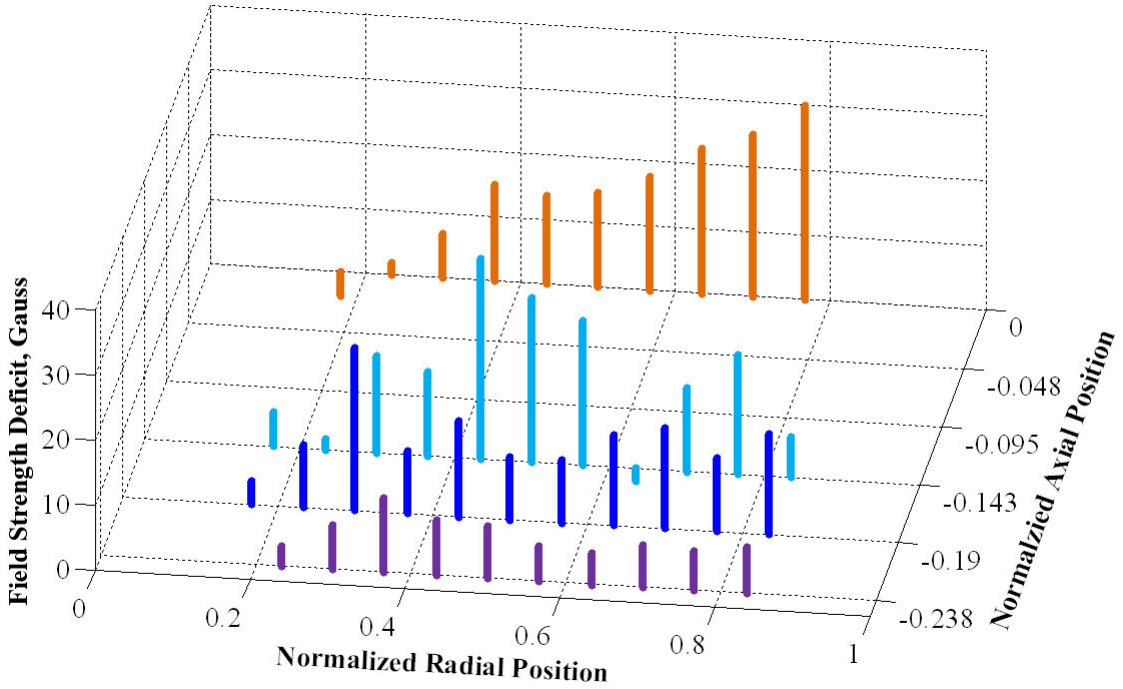

Figure 14. Field strength deficit as a function of normalized position. *Field strength deficit is defined as the in-air minus the in-situ magnetic field strength. Axial position is normalized by the channel length with the exit plane at 0 and the anode at -1. Radial position is normalized by the channel width with the inner wall at 0 and the outer wall at 1.*

Figure 14 shows the field strength deficit as a function of normalized position in one 3D bar plot. From this figure, we can see that the closest match between the in-situ and the in-air magnetic field strengths are found near the walls of the discharge channel. Deviation in field strength near the walls varies from -4 to 7 G, well within the measurement uncertainty. Measurements near the walls are good for validating the Zeeman spectroscopy technique because the Hall current is expected to have little influence at these locations. The in-situ field strength tends to be lower than the in-air field strength by 10-30 G along the centerline of the discharge channel. This difference in field strength tends to be higher downstream (nearer to the exit plane) than upstream (nearer to the anode) in the measurement domain. Unfortunately, the missing data at Z = -0.048 and Z = -0.095 are essential to confirming this trend. Nevertheless, the data fit well with known physics; the Hall current is confined along the channel centerline for a symmetric-magnetic-field thruster, so we should expect the greatest field strength difference along the channel centerline.

D. Hall Current versus Diamagnetic Current

We will now tackle the issue of whether the measured magnetic field strength deficit is primarily induced by the Hall current, the diamagnetic current, or both. If we limit our Hall current calculations to the regions in the Hall thruster where the magnetic field is mostly radial, Eq. (1) can be simplified into Eq. (8),

$$j_{ExB,\theta} \approx \frac{n_e}{B_r}\frac{\partial(eV_P)}{\partial z} \tag{8}$$

where $j_{ExB,\theta}$ is the azimuthual Hall current density, B_r is the radial magnetic field, and V_P is the plasma potential. Similar simplifications can be made to Eq. (3) to form Eq. (9),

$$j_{dia,\theta} \approx -\frac{1}{B_r}\frac{\partial(n_e kT_e)}{\partial z} \tag{9}$$

where $j_{dia,\theta}$ is the azimuthal diamagnetic current density.

Figures 15 and 16 show, respectively, the Hall and diamagnetic current densities as functions of normalized spatial coordinates. The plotted domain encompasses the majority of the Hall and diamagnetic currents as well as the regions plotted in the field strength deficit figures. The data used to generate Figs. 15 and 16 are based on Reid's thesis work involving a fast reciprocating probe system.[15] Electron temperature and ion density were obtained via a Langmuir probe. Electron density was assumed to be roughly the same as ion density due to the quasi-neutrality condition. Plasma potential was obtained with an emissive probe. And magnetic field was measured in air via a Hall probe. Figure 17 shows the total azimuthal current density as a function of normalized space.

From Figs. 15-17, we can see that diamagnetic current does make a sizable contribution but it is relatively weak compare to the Hall current. Fig. 17 looks almost identical to fig. 15 except for a small bump at around Z = -0.12, R = 0.5. Based on these data, we can expect the self-magnetic field measured by LIF to be primarily induced by the Hall current with some contribution from the diamagnetic current.

As it turns out, the diamagnetic current density calculation is dominated by axial gradients in the electron temperature as oppose to gradients in the electron density. In the limit where this is true, Eq. (9) can be rewritten as,

$$j_{dia,\theta} \approx -\frac{n_e}{B_r}\frac{\partial(kT_e)}{\partial z} \qquad (10)$$

where the electron density simply moves outside of the gradient term. An interesting result can be obtained when dividing the absolute value of Eq. (8) by the absolute value of Eq. (10), where both eV_P and kT_e can be written in units of eV.

$$\left|\frac{j_{ExB,\theta}}{j_{dia,\theta}}\right| \approx \left|\frac{\partial(eV_P)}{\partial z} \Big/ \frac{\partial(kT_e)}{\partial z}\right| \qquad (11)$$

The ratio of the Hall current density to the diamagnetic current density is roughly equal to the ratio of the axial gradient of the electrostatic potential energy to that of the electron thermal energy. In a Hall thruster, the electron thermal energy gradient is inherently tied by physical processes to the accelerating potential energy gradient, though the exact relationship is known. But for the moment, if we assume both types of energy vary over the same spatial extend the magnitude of the gradient scales with the peak magnitude of the energy. For this particular Hall thruster and operating condition, the peak electron temperature is ~30 eV and the discharge voltage is 300 V, implying that the Hall current should be about 10 times stronger than the diamagnetic current.

Given the number assumptions made it is unlikely that the ratio of current densities is exactly 10. However, the above exercise shows the physical reason why we should expect the Hall current to dominate over the diamagnetic current for the tested Hall thruster. The Hall current derive energy from the electrostatic field while the diamagnetic current respond primarily to electron thermal gradient. Since the former is always much larger in magnitude than the latter, we can expect the Hall current to dominate over the diamagnetic current.

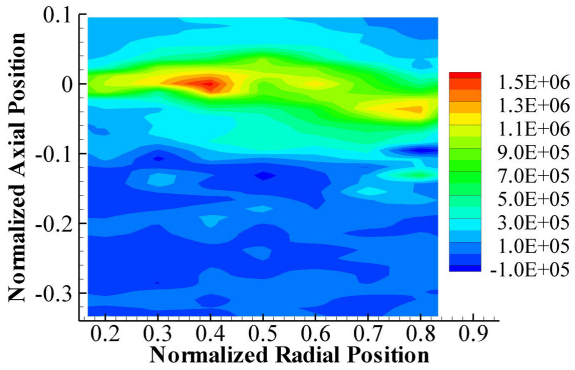

Figure 15. Hall current density.

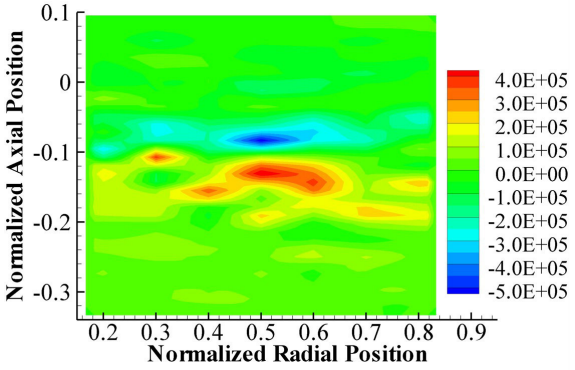

Figure 16. Diamagnetic current density.

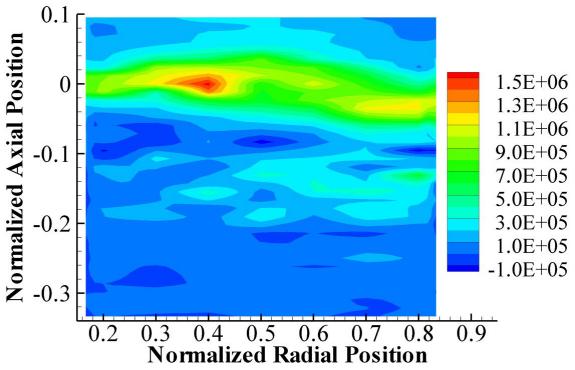

Figure 17. Total azimuthal current density. *Current density in units of A/m^2.*

Note that since the calculated Hall and diamagnetic currents come from a composite of probe measurements the total uncertainty is fairly high. Figs. 15-17 are only meant to show how much relative contribution we should expect from the Hall and diamagnetic currents toward the measured self-field; they are not meant to represent the true magnitude and distribution of the total azimuthual current. Although it would be nice to compute the azimuthual current distribution based on the LIF data and compare it to Fig. 17, we believe we need a more complete set of LIF data to make an accurate comparison. This comparison will be left for future work.

V. Conclusions and Future Works

We have demonstrated the use of a novel optical approach based on magnetic hyperfine splitting to non-intrusively extract magnetic field strength measurements from inside the discharge channel of a 6-kW Hall thruster. Uncertainty in field strength calculated from collected data is ~10 G. In-situ versus in-air field strength measurements show good agreement (<10 G) near the channel walls where the Hall current is expected to have little influence. Measurements near the centerline of the discharge channel show that the in-situ field strength tends to be 10-30 G lower than the in-air Hall probe measurements. Some data were not collected because of an equipment problem, and not because of any issues with the optical technique. This optical technique can easily be adapted toward diagnosing other electric propulsion devices.

The next step in this work is to collect a more complete set of data encompassing the physical region in which the Hall current is expected to have influence. It should be possible to further decrease the uncertainty in the measured field strengths by increasing the SNR and decreasing equipment-related uncertainties. The extent to which the field strength uncertainty can be decreased is unknown at this point. The influence of temperature on the accuracy of the magnetic field measurement will also need to be investigated. Another way to improve this optical technique is to find a transition whose σ-polarized hyperfine structure is even more sensitive to external applied field while the π-polarized structure is still mostly insensitive. This transition should, for the reasons listed in the theories section, be a metastable neutral line.

Acknowledgments

This research is funded by the Air Force Office of Scientific Research (AFOSR) grant FA9550-06-1-0105. The authors would like to thank the AFOSR and Dr. Mitat Birkan, the Project Manager for the said grant.

The authors would like to thank Dr. Timothy B. Smith for his advice on laser-induced fluorescence, Dr. Bryan M. Reid for the fast reciprocating Langmuir and emissive probe data, and Raymond Liang for providing the in-air magnetic field data.

References

[1]Haas, J. M. and Gallimore, A. D., "Considerations on the Role of the Hall Current in a Laboratory-Model Thruster", *37th AIAA/ASME/SAE/ASEE Joint Propulsion Conference & Exhibit*, AIAA-2001-3507, Salt Lake City, UT, 8-11 Jul., 2001.

[2]Hofer, R. R. and Gallimore, A. D., "The Role of Magnetic Field Topography in Improving the Performance of High-Voltage Hall Thrusters", *38th AIAA/ASME/SAE/ASEE Joint Propulsion Conference & Exhibit*, AIAA-2002-4111, Indianapolis, IN, 7-10 Jul., 2002.

[3]Peterson, P. Y., Gallimore, A. D., and Haas, J. M., "An Experimental Investigation of the Internal Magnetic Field Topography of an Operating Hall Thruster", *Physics of Plasmas*, Vol. 9, No. 10, Oct., 2002, pp. 4354-4362.

[4]Smith, T. B., Huang, W., Ngom, B. B., and Gallimore, A. D., "Optogalvanic and Laser-induced Fluorescence Spectroscopy of the Zeeman Effect in Xenon", *30th International Electric Propulsion Conference*, 2007-229, Florence, Italy, 17-20 Sep., 2007.

[5]Ngom, B. B., Smith, T. B., Huang, W., and Gallimore, A. D., "Numerical Simulation of the Zeeman Effect from Laser-induced Fluorescence of Neutral Xenon", *30th International Electric Propulsion Conference*, 2007-254, Florence, Italy, 17-20 Sep., 2007.

[6]Ngom, B. B., Smith, T. B., Huang, W., and Gallimore, A. D., "Numerical Simulation of the Zeeman Effect in Neutral Xenon from NIR Diode-Laser Spectroscopy", *Journal of Applied Physics*, Vol. 104, No. 2, 23 Jul., 2008, pp. 023303.

[7]Huang, W., Drenkow, B., and Gallimore, A. D., "Laser-Induced Fluorescence of Singly-Charged Xenon Inside a 6-kW Hall Thruster", *45th AIAA/ASME/SAE/ASEE Joint Propulsion Conference & Exhibit*, AIAA-2009-5355, Denver, CO, 2-5 Aug., 2009.

[8]Huang, W. and Gallimore, A. D., "Laser-induced Fluorescence Study of Neutral Xenon Flow Evolution inside a 6-kW Hall Thruster", *31st International Electric Propulsion Conference*, 2009-087, Ann Arbor, MI, 20-24 Sep., 2009.

[9]Svanberg, S., *Atomic and Molecular Spectroscopy*, 4th ed., Springer-Verlag, Berlin, 2004.

[10]Suzuki, M., Katoh, K., and Nishimiya, N., "Saturated Absorption Spectroscopy of Xe using a GaAs Semiconductor Laser", *Spectrochimica Acta Part A*, Vol. 58, No. 11, Aug., 2002, pp. 2519-2531.

[11]Jackson, D. A. and Coulombe, M. C., "Isotope Shifts in the Arc Spectrum of Xenon", *Proceedings of the Royal Society of London. Series A, Mathematical and Physical Sciences*, Vol. 338, No. 1614, Jun., 1974, pp. 277-298.

[12]Harkness, H. W. and Heard, J. F., "The Stark Effect for Xenon", *Proceedings of the Royal Society of London. Series A, Containing Papers of a Mathematical and Physical Character*, Vol. 139, No. 838, 1 Feb., 1933, pp. 416-435.

[13]Karimov, R. G. and Klimkin, V. M., "Xe I and Xe II Radiative Lifetimes and Transition Probabilities", *Russian Physics Journal*, Vol. 14, No. 3, Mar., 1971, pp. 308-311.
[14]Coleman, T. F. and Li, Y., "An Interior Trust Region Approach for Nonlinear Minimization Subject to Bounds", *SIAM Journal on Optimization*, Vol. 6, No. 2, May, 1996, pp. 418-445.
[15]Reid, B. M., "The Influence of Neutral Flow Rate in the Operation of Hall Thrusters", Ph.D. Dissertation, Aerospace Engineering, University of Michigan, Ann Arbor, MI, 2008.